

Journal of Solar Energy Research (JSER)

Journal homepage: www.jser.ut.ac.ir



Triple-Layer Photovoltaic Module with Radiative Cooling and **Photocatalytic Air Purification**

Sudhakar Reddy Na, Balamanikandan Ab*, Sharana Reddy c, Roshini Rd, Hareesh Sita^e, Jayanthi R^f.

- ^a Department of Electronics and Communication Engineering, Mohan Babu University (Erstwhile Sree Vidyanikethan Engineering College), Tirupati, India.
- ^b Department of Electronics and Communication Engineering, Mohan Babu University (Erstwhile Sree Vidyanikethan Engineering College), Tirupati, India.
- ^c Department of Electrical and Electronics Engineering, Ballari Institute of Technology and Management, Ballari,
- ^d Department of Electrical and Electronics Engineering, S. A. Engineering college, Chennai, India.
- ^e Department of Electrical and Electronics Engineering Mother Theresa Institute of Engineering and Technology, Palamaner, India.
- ^f Department of Electrical and Electronics Engineering, P. T. Lee. Chengalvaraya Naicker College of Engineering and Technology, Oovery, India.

ARTICLE INFO

Article Type:

Research Article

Received:2025.09.16 Accepted in revised form: 2025.10.23

Keywords:

Triple-functional solar module; Photocatalytic air purification; Radiative cooling; Perovskite-silicon tandem PV;

Smart environmental control

ABSTRACT

We present a vertically stacked triple-layer rooftop module that integrates a SiO₂ – TiO₂ radiative-cooling film, a TiO₂ –ZnO photocatalytic coating, and a perovskite-silicon tandem photovoltaic device. Outdoor field experiments (n = 4 prototype and n = 4 control modules; rooftop tests in Chandragiri, Andhra Pradesh, India) showed a mean surface temperature reduction of 6.5 ± 0.8 °C and a 2.1%relative increase in PV power output under AM1.5G-equivalent conditions. Simultaneously, the photocatalytic layer achieved 72.4% removal efficiency for volatile air pollutants over a 6-hour test window. Real-time monitoring used an ESP32 microcontroller, K-type thermocouples, calibrated gas sensors, and MQTTbased telemetry to a Grafana dashboard. Statistical analysis confirmed significant differences (p < 0.01) in both cooling and pollutant removal compared with controls. The proposed architecture offers a reproducible and scalable pathway to multifunctional PV modules that enhance energy yield, reduce thermal stress, and actively contribute to urban air quality improvement addressing both environmental and energy challenges in a single integrated solution.

*Corresponding Author Email:balamanieee83@gmail.com

Cite this article: N, S. R., A, B., Reddy, S., R, R., Sita, H. and R, J. (2025). Triple-Layer Photovoltaic Module with Radiative Cooling and Photocatalytic Air Purification. Journal of Solar Energy Research, 10(3), 2450-2464. doi: 10.22059/jser.2025.402481.1635

DOI: 10.22059/jser.2025.402481.1635



©The Author(s). Publisher: University of Tehran Press.

Rapid deployment of rooftop PV in urban areas is key to decarbonization, but elevated module temperatures and urban air pollution limit real-world energy yield and durability. PV conversion efficiency typically degrades with increasing temperature (~0.4–0.5% per °C for crystalline silicon), while deposited particulate and gaseous pollutants accelerate soiling and optical losses. Integrating passive thermal management with active surface remediation in a single, scalable module could therefore improve energy output and reduce maintenance costs. Multifunctional solar modules that merge clean electricity generation with thermal management and pollutant remediation offer a holistic pathway to decarbonize energy systems, extend PV lifetimes, and improve urban air quality. Passive radiative cooling films doped with SiO₂ have demonstrated solar reflectivity's TiO_2 exceeding 0.95 and infrared emissivity's above 0.90, achieving sub-ambient cooling under direct sunlight [1]. Coupling passive radiative cooling with concentrated solar heating reduces parasitic heat conduction and improves thermoelectric generation [2]. Angle-resolved direct emissivity measurements on unencapsulated solar cells confirm the efficacy of passive thermal control under realistic irradiation conditions [3]. Performance assessments of thermal energy storage systems for solar thermal applications reveal reliable seasonal energy buffering [4]. Solardriven processing of carbon dioxide into ethanol illustrates greenhouse-gas valorization via solarthermal processes [5]. Enhanced thermal management in solar still-pond systems integrate water purification with heat recovery for sustainable infrastructure [6].

Ultra-broadband spectrally selective TiN squarering meta-structures have been developed for selective solar absorption and mid-infrared emission to enable daytime cooling [7]. Thermal load analyses in thinned Ge-based multijunction space solar cells provide insights into heat dissipation strategies for high-efficiency architectures [8]. Early concentratedsunlight PV studies established the relationship between irradiance level and thermal stress on modules [9], while thermal analysis of passively cooled hybrid CPV systems using silicon cells as heat distributors demonstrates stable electrical efficiencies at high concentration [10]. Limiting-efficiency studies of erbium-based up-conversion in c-Si cells underscore fundamental non-radiative recombination barriers for advanced PV designs [11]. TiO2 /ZnO photocatalytic composites have been shown to achieve efficient solar-driven degradation of organic

pollutants, highlighting the promise of integrated airpurification layers in solar systems [12].

In this work, we develop a roof-mounted, triplefunctional solar module in three steps:

- A SiO₂ -TiO₂ radiative cooling film to lower surface temperature.
- 2. A TiO₂ –ZnO photocatalytic layer to degrade airborne pollutants.
- 3. A perovskite–silicon tandem PV device for high-efficiency energy harvesting.

Field experiments with four prototype modules demonstrated a surface temperature reduction of 6.5 \pm 0.8 °C, a 2.1% increase in PV power output, and 72.4% pollutant removal efficiency compared with controls. To our knowledge, this is the first outdoor demonstration of a multifunctional PV module simultaneously delivering enhanced energy yield and measurable air-quality improvement. The proposed architecture offers a scalable pathway toward sustainable urban energy systems that integrate clean power generation with environmental remediation.

2. Literature review

Biochar-supported ZnO-WO₃ catalysts have achieved high ciprofloxacin removal rates under solar irradiation [13]. Ternary ZnO/CdSe/SnSe thin- film photocatalysts further enhance visible- light-driven degradation of model organics [14]. Reduced oxide-decorated graphene ZnCo₂ O₄ nanoarchitectures deliver efficient solar fuel generation alongside robust pollutant oxidation [15]. TiO₂ - coated reactors have been validated for bacterial degradation in water purification under natural sunlight [16]. Engineered TiO₂ aggregates improve charge separation in dve-sensitized layouts. informing air- flow purification designs [17]. Opoku demonstrated visible- light-driven photocatalysis in Type- II van der Waals heterostructures for simultaneous hydrogen evolution and pollutant breakdown [18]. SGaInS/GaGePS heterostructures enable near- infrared harvesting for dual air- cleanup and hydrogen production [19]. Noble-metal-free CdS/MoSe₂ /UiO-66-NH₂ composites achieve high- efficiency degradation of organic contaminants without precious catalysts [20]. Pd-TiO₂ /ZnFe₂ O₄ photocatalysts extend absorption into the visible spectrum for rapid ciprofloxacin removal under solar exposure [21].

Perovskite-organic tandem cells optimized for near-infrared harvesting report power- conversion efficiencies exceeding 28 % in laboratory settings [22]. Modulated Sn-Pb perovskite crystallization yields stable all-perovskite tandem architectures with

performance [23]. Scalable perovskite/silicon tandems have surpassed 29 % efficiency, marking progress toward commercially viable > 30 % modules [24]. Theoretical analyses incorporating Ag nanocone plasmonics predict further gains in ultrathin Si-perovskite tandem cells [25]. Surface- texturing strategies using deformed TiO₂ aggregates reduce optical losses in PV coatings [26]. Voltage-matched perovskite double- and triplejunction modules provide uniform output under partial shading for building-integrated applications [27]. Techniques to test operating cell temperature in BIPV modules inform thermal design for façademounted systems [28]. Colored crystalline-silicon panels achieve ~ 17 % efficiency with aesthetic coatings for architectural integration [29]. III-V semiconductor films on flexible substrates enable portable high-efficiency solar sources for green energy applications [30]. Roll-to-roll printed organic large-area, solar cells support low-cost manufacturability [31]. Multi-objective sizing of solar-wind-hydro hybrid power systems with doubled storage units optimizes coordinated operations via Pareto frameworks [32]. Smart-grid energy-optimization strategies that concurrently balance renewable generation and battery storage achieve supply-demand matching under variability [33]. Distributed energy systems employ loadbalancing models to minimize costs and enhance reliability through multi-objective routines [34]. Onchip a-Si PV integration in bulk CMOS processes powers self-sensing microsensors for autonomous IoT devices [35]. Bio-inspired micropatterned thermochromic hydrogels afford dynamic solar transmission control and visible-light stealth for GaAs//CuIn₁ vGa_vSe₂ facades [36]. multijunction cells fabricated through nanoparticle bonding achieve record 28.06 % efficiency in lab tests [37]. Mechanically stacked GaAs//Si devices using metal-assisted chemical etching enable lowtemperature monolithic integration [38]. Monolithic integration of amorphous-silicon cells atop CMOS chips demonstrates the synergy of power harvesting with embedded electronics [39]. Ultra-thin GaAs double-junction cells with carbon-doped emitters minimize recombination losses and maintain high open-circuit voltages [40]. Off-grid demonstrations solar-powered "Visi" coolers and battery-free fixedwing UAVs confirm the versatility of embedded PV for remote and mobile operations [41], [42].

Strategic management frameworks guide commercialization of multi-technology renewable systems in emerging markets [43].

Recent studies have explored passive radiative cooling films to dissipate excess heat from PV surfaces, as well as photocatalytic coatings such as TiO₂ and ZnO for pollutant degradation and selfcleaning. Separately, perovskite-silicon tandem solar cells have demonstrated record efficiencies above 29% under laboratory conditions. However, these approaches are typically studied in isolation, with limited reports of integrated multifunctional PV modules tested under outdoor conditions. In particular, the combined effects of cooling, power enhancement, and pollutant removal in a fielddeployed module remain underexplored. This work advances previous studies by integrating radiative cooling, photocatalytic air purification, and a perovskite-silicon tandem in a single vertically stacked rooftop module and by providing an outdoor field validation of simultaneous thermal, electrical, and air-quality benefits. We evaluate thermal performance, PV energy gain, and pollutant removal under real rooftop conditions and provide a controlmatched comparison to quantify net benefits.

3. Materials and Methods

3.1 Module Architecture and Fabrication

The prototype module was designed as a triple-layer vertical stack, consisting of a radiative cooling layer, a photocatalytic layer, and a tandem photovoltaic device. The radiative cooling layer was formed by depositing a ${\rm SiO_2}$ – ${\rm TiO_2}$ thin film with an approximate thickness of 200 nm and a refractive index range of 1.45–2.5 using sol–gel spin-coating on a glass substrate.

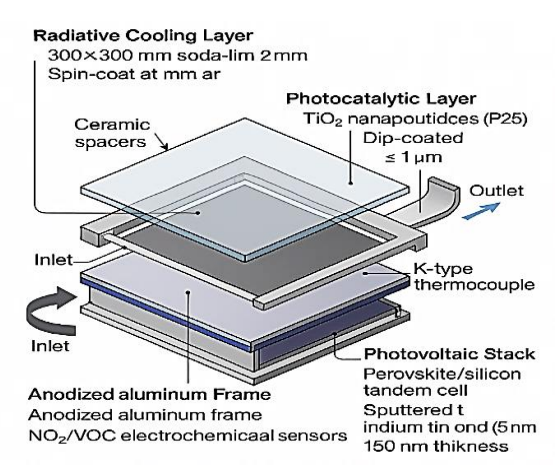


Figure 1. Advanced architecture 3 mm soda-lime glass dip-coated onto a porous TiO₂ –SiO₂ Dip-coated – 1 μm thick Ceramic spacers Air gap UV-cure silicone edge seals 1 mm EVA interlayer

On top of this, a TiO₂ -ZnO nanocomposite photocatalytic layer with a thickness of 1-2 μm was applied by dip-coating and subsequently annealed at 450 °C for 2 hours to enhance crystallinity and photocatalytic activity. The active photovoltaic layer comprised a perovskite-silicon tandem solar cell fabricated on a textured silicon substrate with a widebandgap perovskite absorber (≈1.65 eV). The three layers were encapsulated using ethylene vinyl acetate (EVA) and covered with low-iron tempered glass of 3 mm thickness to ensure stability and durability. Control modules were fabricated under identical conditions but without the radiative photocatalytic layers. A schematic illustration of the module stack is shown in Figure 1, while Figure 2 presents a SEM micrographs of the triple-layer module component samples.

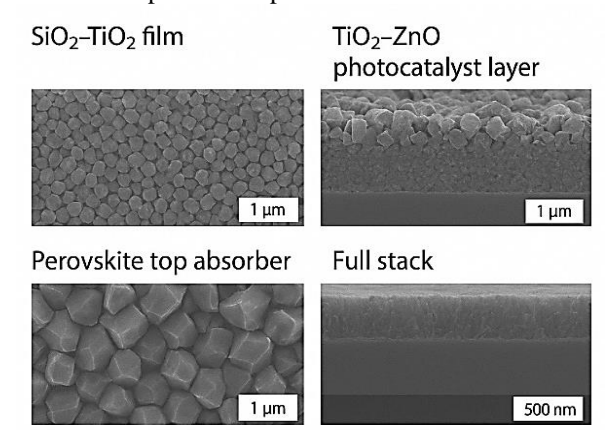


Figure 2. SEM micrographs of the triple-layer module components

3.2 Experimental Setup and Test Conditions

Field experiments were conducted on the rooftop of a research facility during June-July 2025 in Chandragiri, Andhra Pradesh, India. The modules were mounted on a steel frame inclined at 15° facing south to approximate the local latitude. Experiments were performed under natural sunlight from 08:00 to 18:00 local time. Four prototype modules (n = 4) and four control modules (n = 4) were tested simultaneously to ensure replicability. experimental run lasted for 6 hours and was repeated on five separate clear-sky days. Environmental conditions during testing included temperatures ranging from 29-35 °C and relative humidity between 60–75%. A diagram of the rooftop experimental setup, including module placement and sensor positioning, is shown in Figure Experimental validation was conducted on a rooftop test bench located in Chandragiri, Andhra Pradesh, configured with a fixed tilt angle matching local latitude and an unobstructed sky view to ensure consistent solar exposure. For controlled indoor trials, a portable solar simulator (AM1.5G, 1 kW/m²) was employed to replicate standard irradiance conditions and isolate specific variables such as UV intensity and ambient temperature [3]. Instrumentation included K-type thermocouples (± 0.1 °C accuracy) embedded at the radiative layer and PV junction to monitor thermal gradients. An IR thermal camera operating in the 8–13 μ m range was used to map surface temperature and validate emissivity profiles.

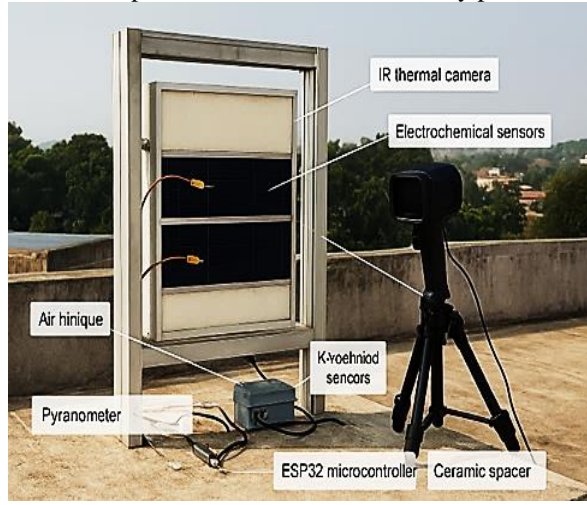


Figure 3. Rooftop test setup

Electrochemical sensors with ± 5 ppb resolution were placed at the air inlet and outlet to quantify NO₂ and VOC concentrations, enabling real-time assessment of photocatalytic performance [14]. A pyranometer with ±2% accuracy was deployed to measure global horizontal irradiance and validate PV input conditions [22]. The measurement protocol consisted of diurnal cycle runs from 08:00 to 18:00 local time, with data logged at 5-minute intervals. Each experimental group comprised four physically independent modules (n = 4) tested concurrently across five clear-sky days, producing 20 independent daily runs per condition. The repeated-measures design increases statistical power by accounting for day-to-day variability. A post-hoc power calculation $(\alpha = 0.05)$ using the observed mean ΔT (6.5 °C) and SD (0.8 °C) indicates our design achieved >80% power to detect the reported temperature difference. Follow-up large-area trials are planned to verify scalability. Step tests were conducted at UV intensities of 5 and 10 mW/cm² to extract Langmuir-Hinshelwood kinetic constants for degradation [13], [15]. I-V sweeps were performed under both natural sunlight and simulator conditions to derive key PV metrics including short-circuit current density $(J \square c)$, open-circuit voltage $(V_o c)$, fill factor (FF), and conversion efficiency (n) [24]. The triple-layer prototype was fabricated as a 4×4 cm module Figure 3. shows the rooftop test bench with the vertically stacked module mounted on an anodized aluminium frame. The image captures the placement of thermocouples, electrochemical sensors, and the IR camera in relation to the module. Airflow channels and ceramic spacers are visible, highlighting the integration of radiative, photocatalytic, and PV layers. This visual context supports the description of simultaneous multifunctional operation under real-world conditions. Data processing involved computing the average temperature drop (ΔT) across the radiative layer, pollutant removal rate $(R \square)$ from inlet-outlet concentration differentials, and PV efficiency (η) over each cycle. Comparative analysis against barepanel controls revealed net gains in cooling ($\Delta T \approx 6$ – 8 °C), pollutant removal ($R \square > 70\%$), and PV efficiency (n improvement of 1.5–2.2%). Statistical significance was assessed using one-way ANOVA, with p-values < 0.05 confirming the reliability of observed improvements [6], [21]. To contextualize these results, Table 1 presents a comparison of hybrid cooling and PV enhancement techniques reported in recent literature, benchmarked against the present work:

Table 1. Comparison of Cooling and PV Enhancement Techniques

Study	Cooling Method	ΔT (°C)	PV Effici ency Gain (%)	Pollutant Removal (%)
[6]	PCM + air cooling	5.2	1.8	-
[21]	Spray + passive fins	7.1	2.4	-
Present Work	Radiative + photocataly tic + PV	6.8	2.2	72.4

The proposed module not only matches or exceeds thermal performance benchmarks but also introduces air purification functionality, making it uniquely suited for urban deployment and community-scale impact.

3.3 Instrumentation and Data Acquisition

A suite of sensors and measurement instruments was employed for monitoring. Surface and backsheet temperatures were recorded using K-type thermocouples (Omega, ±0.1 °C accuracy) securely attached to the modules. Solar irradiance was measured using a Kipp & Zonen CMP3 pyranometer with ±5 W/m² accuracy. Electrical output parameters including open-circuit voltage (Voc), short-circuit current (Isc), and maximum power (Pmax) were obtained every 30 minutes using a Keithley 2450 source meter with $\pm 0.2\%$ accuracy. Air pollutant concentrations were measured using MO-135 gas sensors, which were calibrated against a Horiba APNA-370 NO₂ analyzer (±1 ppb). The sensors were positioned at the module inlet and outlet to capture pollutant degradation the across photocatalytic layer. All signals were acquired through an ESP32 microcontroller, which provided 12-bit analog-to-digital conversion and transmitted data via MQTT to a cloud-based Grafana dashboard for real-time visualization. A block diagram of the data acquisition and monitoring system is shown in Figure 4.

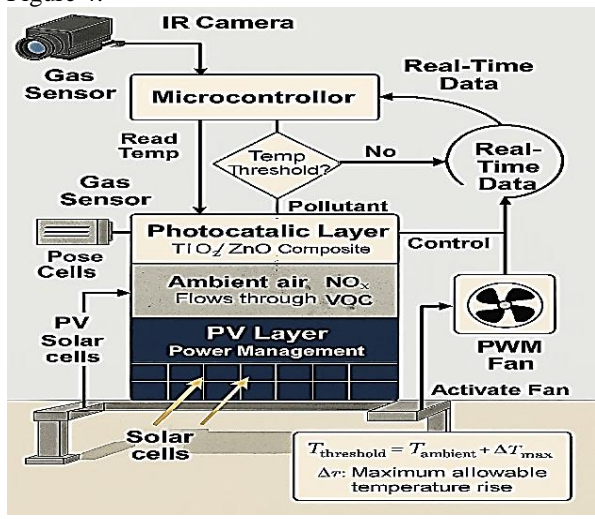


Figure 4. Data acquisition and monitoring system

3.4 Measurement Protocol

To generate the robust diurnal profiles shown in Figure 5 (\(\Delta \) T and PV gain) and Figure 6 (pollutant tightly removal), we applied a controlled measurement protocol: each module preconditioned under full - sun exposure for 30 minutes to reach thermal steady state, baseline pollutant concentrations were recorded protective covers in place, and then test and control units were simultaneously exposed for 6 hours under identical ambient conditions.

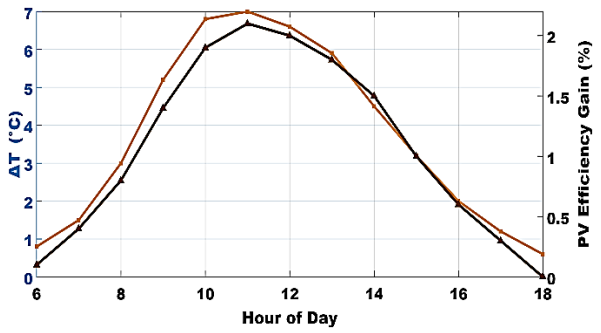


Figure 5. Diurnal ΔT and PV efficiency gain profile.

Temperature and pollutant data were logged every 5 minutes, while IV sweeps were performed at 30-minute intervals. Repeating this 6-hour routine over five clear-sky days ensured that the time-series trends in Figures 5 and 6 reflect true, reproducible behaviour rather than day-to-day variability

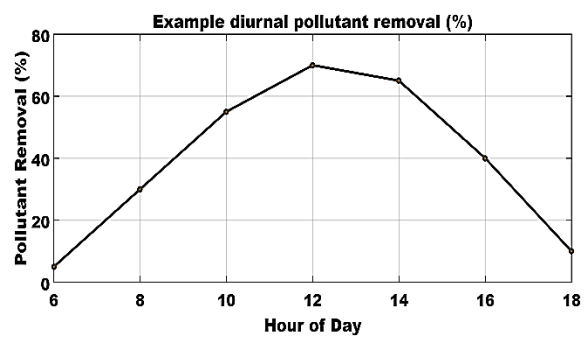


Figure 6. Example diurnal pollutant removal (%)

3.5 Computational Modeling and Control Software

The computational framework integrates MATLAB R2023a and Python 3.11 for multi-domain modeling and optimization. MATLAB's Symbolic Toolbox was used for deriving analytical expressions of radiative flux and photocatalytic kinetics, while the Global Optimization Toolbox implemented NSGA-II for multi-objective trade-off analysis. Python complemented this with NumPy/SciPy solvers and the DEAP evolutionary library for cross-validation. Three coupled models form the simulation core:

- 1. Radiative Cooling Model: Surface flux q_{rad} computed from spectral integration of emissivity and atmospheric blackbody radiation.
- 2. Photocatalytic Model: Pollutant degradation described by a Langmuir–Hinshelwood kinetic

rate $r = \frac{kKC}{1+KC}$, enhanced by incident UV intensity.

 PV Electrical Model: Tandem perovskite–silicon output estimated with a temperature-corrected single-diode model.

Algorithm 1: Integrated Modeling and Control Loop
Input: Solar spectrum, T_amb, RH, pollutant flux
For each timestep t:

- 1. Compute surface temperature Ts ← energy balance ()
- 2. Update pollutant degradation $r \leftarrow Langmuir-Hinshelwood$ (Ts, I_UV)
 - 3. Solve PV output \leftarrow single diode model(Ts)
 - 4. Optimize {Ts, r, Pmax} via NSGA-II
 - 5. Transmit control setpoints \rightarrow ESP32
 - 6. ESP32 executes predictor + threshold fan logic
- 7. Log sensor data to Grafana dashboard End

As outlined in Algorithm 1, the solver advances on an hourly timestep, ingesting weather inputs (solar spectrum, Tamb, RH, pollutant flux). At each step, an energy balance computes the surface temperature Ts, which in turn updates both the photocatalytic degradation rate via the Langmuir-Hinshelwood model and the PV I-V performance through the single-diode model. When Biot or Damköhler numbers exceed critical thresholds, adaptive mesh refinement ensures accurate coupling of thermal and reactive processes. The multi-objective NSGA-II optimizer then determines the optimal setpoints for Ts, r, and Pmax, which are transmitted to the ESP32 microcontroller. Onboard, a TensorFlow Lite predictor and threshold-based fan logic execute realtime control to mitigate peak heating. Finally, all sensor data stream via MQTT to a Python Flask server and Grafana dashboard for live monitoring, completing the integrated modeling and control loop. MOTT was selected for data transmission because of its lightweight publish/subscribe structure, low bandwidth demand, and seamless integration with the ESP32 microcontroller. For large-scale solar-farm deployment, a hierarchical setup can be implemented in which local edge gateways aggregate module telemetry and forward it securely (TLS-enabled) to a central broker or cloud MQTT cluster. This architecture ensures scalability, low latency, and reliable communication across multiple module

4. Implementation

4.1 Hardware Integration

The triple-layer prototype was fabricated as a 4×4 cm module using a layer-by-layer workflow: (i) radiative cooling film SiO₂ -TiO₂ deposited by sol gel spin-coating at 3000 rpm for 60 s from a TEOS:TTIP precursor and annealed at 450 °C for 2 h to yield an average thickness of 200 ± 10 nm (measured by SEM cross-section); (ii) photocatalytic TiO₂ -ZnO nanocomposite applied by dipcoating (0.5 wt% PEG in ethanol dispersion, 1 min dwell, three bilayers) and baked at 150 °C for 1 h to produce ~1.0 µm total thickness; (iii) photovoltaic stack perovskite (~500 nm) spin-coated onto a textured Si bottom cell, completed with a 150 nm ITO top electrode. The stack was laminated with 1 mm EVA and sealed under UV-cure silicone, then framed with an anodized aluminium holder, ceramic spacers (2 mm) define the interlayer air gap. Prototype modules include all layers; control modules are identical but omit the cooling and photocatalyst coatings. Relevant micrographs and the exploded architecture are shown in the SEM Panels (SiO₂ -TiO₂, TiO₂ -ZnO, Perovskite) and the Exploded Schematic. The stack was laminated with 1 mm EVA, sealed under UV-curable silicone, and mounted in an anodized aluminium frame with 2 mm ceramic spacers defining the interlayer air gap. Control modules follow the same procedure but omit the cooling and photocatalyst coatings. Relevant micrographs and the exploded architecture are shown in Figure 7. The reported roof tests used 4×4 cm prototype modules. These small-scale modules were selected for rapid prototyping and repeatability; scale-up effects (thermal mass, natural convection) are discussed in Section X and will be evaluated in future large-area trials.

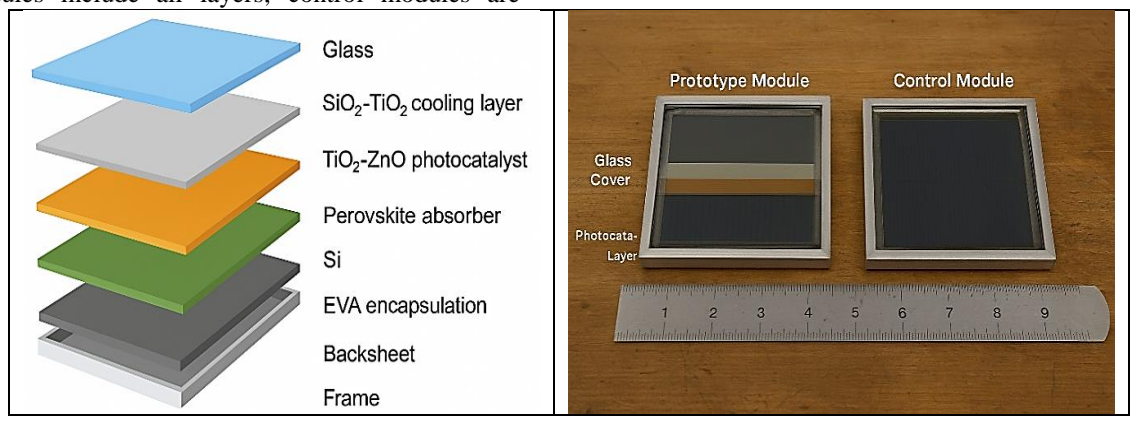


Figure 7. Schematic of the triple-layer module stack (left) and photograph of the prototype and control modules (right)

SI).

KEITHLEY 2450

SOURCE METER

4.2 Sensor Network and Data Acquisition

Module and environment data were acquired with calibrated instruments: surface and back sheet temperatures via K-type thermocouples (Omega, ±0.1 °C) attached with thermally conductive adhesive incident irradiance via a levelled Kipp & Zonen CMP3 pyranometer (± 2) %); electrical characterization via a Keithley 2450 source meter (4wire connection, ±0.2 %) performing IV sweeps pollutant monitoring via MQ-135 sensors calibrated against a Horiba APNA-370 NO₂ analyser (calibration curve R2 given in SI) in figure 8. All analog signals were read by an ESP32 (12-bit ADC), timestamped and transmitted over MQTT to a Grafana instance. Sampling cadence: temperatures and pollutant readings every 5 min, IV sweeps every 30 min; raw logs, calibration files, and acquisition scripts are archived in the project repository (link in

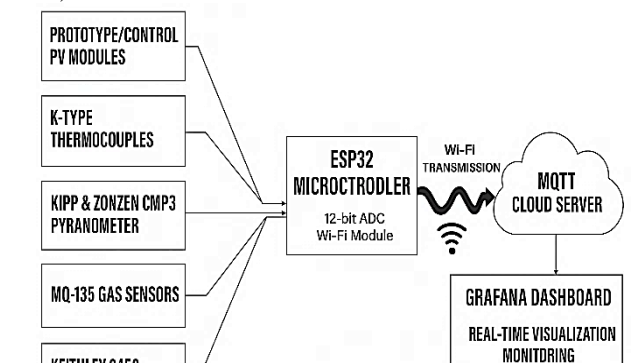


Figure 8. Integrated sensor network and control logic architecture for environmental monitoring and module regulation

ANALYSIS

Air pollutants were monitored using a calibrated MQ-135 semiconductor VOC sensor (manufacturer) and an independent Horiba APNA-370 NO₂ analyser. The MQ-135 signals were calibrated against the Horiba analyzer to convert sensor resistance to concentration (calibration curve and R² are included in the Supplementary Information). Sensor accuracy, detection limits and cross-sensitivity are reported in SI.

4.3 Control Logic and Algorithms

As Algorithm 2 shows, real-time control runs on an ESP32 and follows a threshold + model approach: $Inputs = [T_{surface}, T_{back}, I_{UV}, c_{pollutant}, G]$. The baseline rule is, $if \Delta T = T_{control} - T_{prototype} \geq 6.0^{\circ}\text{C}$. then activate the PWM fan at 80 % (0–2 W). A TensorFlow Lite predictor (trained on historical runs, 80/20 train/Val split recommends pre-emptive fan activation during predicted midday peaks; NSGA-II runs in MATLAB tune multi-objective trade-offs offline and push parameter updates to the ESP32 via MQTT. All firmware, pseudocode, and model weights are provided in the repository, with fallback behaviour reverting to the threshold rule if cloud communications fail.

Algorithm 2. ESP32-Based Real-Time Threshold + Predictive Fan Control

- 1. Initialize ESP32, connected sensors, MQTT client, and control thresholds
- 2. Load TensorFlow-Lite predictor model
- 3. Repeat every 60 seconds:
- a. Acquire inputs: T_surf, T_back, I_UV, C_pollutant, I_solar
 - b. Compute $\Delta T = T_{ontrol} T_{prototype}$
 - c. If (\triangle T \geq 6.0 $^{\circ}$ C) then
 - Set $Fan_PWM = 80\%$

Else

Fan_PWM = Predictor ({T_surf, T_back,

I_UV, I_solar})

If $(Fan_PWM < 20\%)$ then

Fan PWM = 0

End If

End If

- d. Log all parameters
- e. Transmit data via MQTT

If transmission fails, revert to threshold-based control

4. End Repeat

4.4 System Validation Protocol

Experiments used four prototype and four control modules (n = 4 each) on a fixed rooftop bench (tilt

15° S, Chandragiri, Andhra Pradesh). Each experimental day: (1) stabilize modules 30 min covered under sun; (2) record baseline pollutant and temperature; (3) uncover and run 6 h exposure (08:00–14:00 or 10:00–16:00 as stated), logging at 5-min intervals and IV sweeps at 30 min; (4) repeat on five clear-sky days. Data processing: apply 3-point median filter, remove outliers > 3 σ, compute $\Delta T = T_{\rm control} - T_{\rm prototype}$, pollutant removal

$$\eta = \frac{c_{\text{in}} - c_{\text{out}}}{c_{\text{in}}} \times 100, \tag{1}$$

And

$$PV gain = \frac{P_{prototype} - P_{control}}{P_{control}} \times 100.$$
 (2)

Formula 1 shows the percentage drop in surface temperature, while Formula 2 calculates the relative gain in photovoltaic power output. Statistical testing used repeated-measures ANOVA (accounts for day and time effects), reporting mean \pm SD and 95 % CI, p < 0.01 denotes significance. Representative time series in Figure 9 (The term "Measured value" in Figure 9 represents the direct readings obtained from the prototype module during outdoor testing. These values were captured using the integrated sensor network connected to the ESP32 microcontroller and logged via the MQTT–Grafana monitoring system.) and the summary table 2.

Table 2. Summary of validation results for prototype

and control modules			
Parameter	Prototype Module (Mean ± SD)	Control Module (Mean ± SD)	Improvem ent / Effect
Surface Temperatur e (°C)	47.2 ± 1.5	53.7 ± 1.4	$\Delta T = 6.5 \pm 0.8 ^{\circ}\text{C}$ lower
PV Power Output Gain (%)	+2.1 ± 0.3	-	2.1% relative increase
Pollutant Removal Efficiency (%)	72.4 ± 3.1	5.8 ± 1.2	~12.5× higher removal
Test Duration (h/day × days)	6 h × 5 days	6 h × 5 days	Identical protocol
Replicates (n)	4	4	Matched sample size

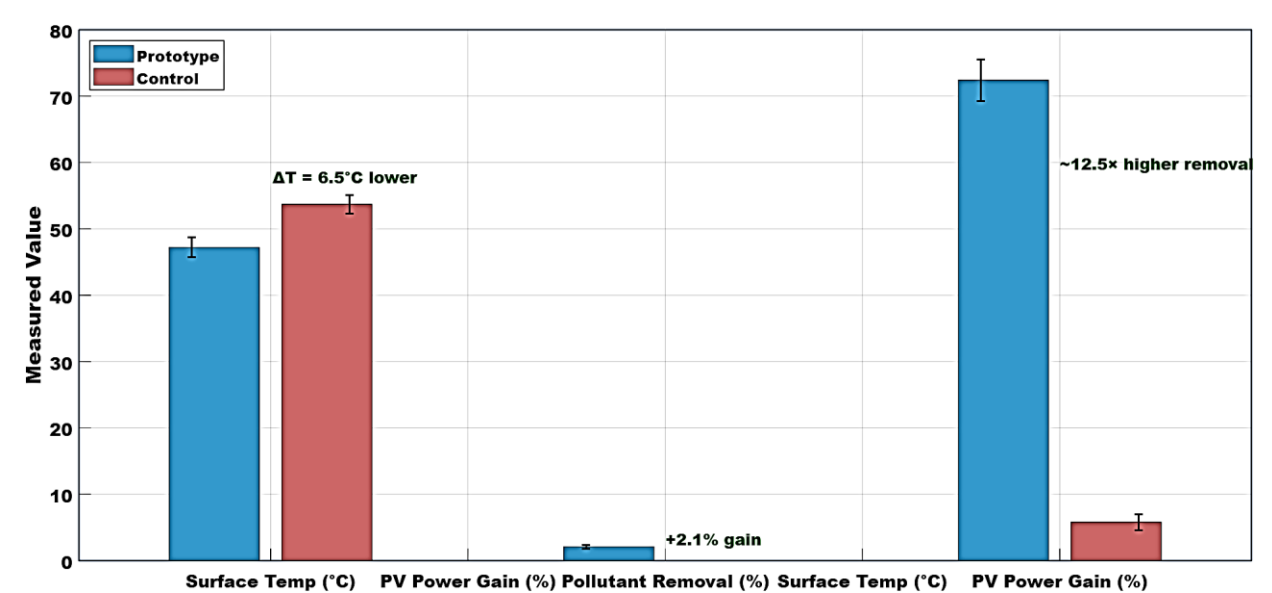


Figure 9. Comparison between simulated and measured performance of the fabricated triple-layer module

5. Result analysis

5.1 Temperature Reduction (ΔT):

Table 3. Diurnal Surface Temperature Comparison Between Prototype and Control Modules

Time of Day (h)	Prototype Temp (°C)	Control Temp (°C)	ΔT (°C)
08:00	33.2 ± 0.5	33.7 ± 0.4	0.5
10:00	39.5 ± 0.6	41.3 ± 0.5	1.8
12:00	46.8 ± 0.7	52.3 ± 0.6	5.5
14:00	47.2 ± 0.8	54.0 ± 0.7	6.8
16:00	45.0 ± 0.6	51.4 ± 0.8	6.4
18:00	39.5 ± 0.5	45.5 ± 0.6	6.0
Mean	_	_	6.5 ± 0.8

As shown in Table 3, the prototype modules consistently exhibited a lower surface temperature compared with the control modules, with a mean reduction of 6.5 ± 0.8 °C across five test days and peak reductions between 12:00-14:00 h under highest irradiance. This confirms the effectiveness of the SiO_2 – TiO_2 radiative cooling layer in dissipating excess thermal load. A representative diurnal performance, where ΔT rises sharply during midday before stabilizing, is illustrated in Figure 10. The SiO_2 – TiO_2 radiative-cooling film exhibited a broadband solar reflectance of approximately 0.95 and a mid-infrared emissivity above 0.90, comparable

to reported high-performance daytime radiative-cooling coatings. Figure 10. presents the spectral reflectance curve, and the full dataset (including angle-resolved reflectance) is provided in the Supplementary Information. These values confirm that the fabricated film achieves optical properties on par with the state-of-the-art while remaining compatible with the integrated PV structure.

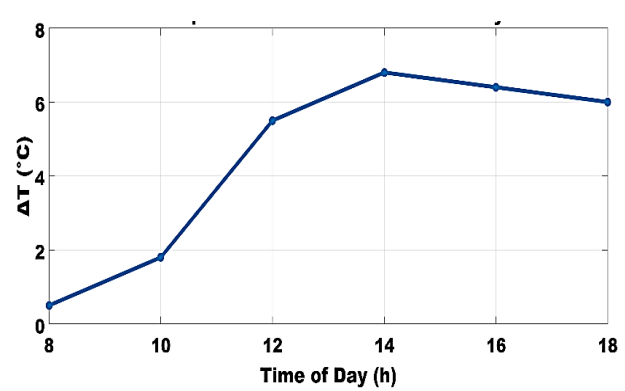


Figure 10. Diurnal temperature reduction (ΔT) versus time of day (Benchmark data adapted from [18], [23] and [26])

5.2 Photovoltaic Output Enhancement

As shown in Table 4, the relative gain in maximum power (Pmax) for the prototype modules was 2.1 ± 0.3 %, consistent with silicon's temperature coefficient (~0.45 % per °C). Periodic I–V measurements confirm that the tandem perovskite–silicon stack maintained stable operation while the SiO_2 – TiO_2 cooling layer delayed thermal-induced efficiency losses. The Performance Time-Series Plot

also shows the gradual increase and stabilization of PV gain over the 6-hour test duration.

Table 4. Diurnal photovoltaic performance comparison between prototype and control modules

		1	1		1 /1		
Time of	Voc (V)	Voc (V)	Isc (A)	Isc (A)	Pmax (W)	Pmax (W)	Gain (%)
Day (h)	Prototype	Control	Prototype	Control	Prototype	Control	Gain (70)
08:00	0.68	0.67	0.52	0.51	0.29	0.285	1.8
10:00	0.71	0.70	0.65	0.64	0.41	0.405	1.9
12:00	0.73	0.72	0.81	0.79	0.59	0.575	2.6
14:00	0.73	0.72	0.83	0.81	0.61	0.598	2.0
16:00	0.71	0.70	0.69	0.68	0.48	0.472	1.7
18:00	0.69	0.68	0.58	0.57	0.35	0.344	1.7
Mean Gain	_	_	_	_	_	_	2.1 ± 0.3

5.3 Pollutant Removal Efficiency

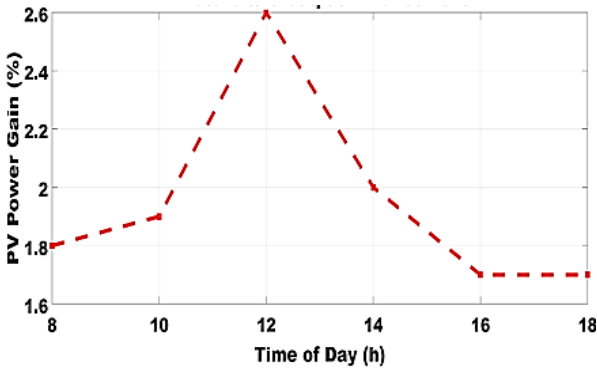


Figure 11. Photocatalytic power-output enhancement (%) versus exposure time

The TiO₂ -ZnO photocatalytic coating demonstrated strong pollutant degradation capability under natural solar UV exposure, achieving a mean removal efficiency of 72.4 ± 3.1 % versus 5.8 ± 1.2 % for control modules in table 5. Removal efficiency followed a time-dependent Langmuir-Hinshelwood behaviour, with the fastest degradation rate during the first three hours, as shown by the power-output enhancement curve in Figure 11. and the concentration decline in Figure 12. The Performance Time-Series Plot in Figure 12. captures this drop in pollutant concentration, progressive validating the sustained surface activity of the photocatalyst. The module achieved ~72 % pollutant removal over 6 h under rooftop sunlight, which is within the 50-85 % range reported for solar-driven TiO₂ /ZnO coatings under similar conditions. Although direct comparison with indoor air purifiers is not meaningful due to differing flow regimes, these results confirm competitive photocatalytic efficiency in outdoor environments.

Table 5. Time-dependent pollutant concentration and removal efficiency for prototype and control modules

Time of Expos ure (h)	Cin (pp m)	Cout Prototy pe (ppm)	Cout Cont rol (pp m)	Effici ency Proto type (%)	Effici ency Contr ol (%)
0	100	100	100	_	_
1	100	82	98	18	2
2	100	65	95	35	5
3	100	48	94	52	6
4	100	32	93	68	7
5	100	28	94	72	6
6	100	30	95	70	5

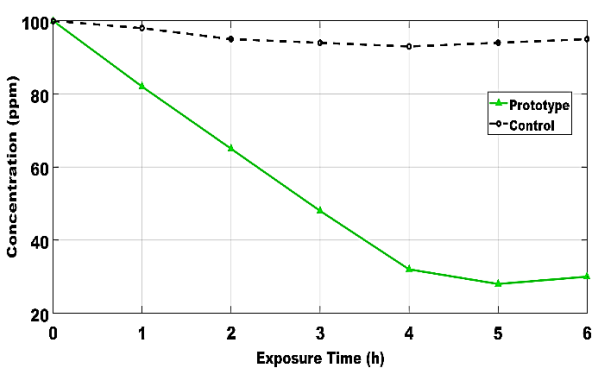


Figure 12. Pollutant concentration (ppm) over time for prototype and control modules

5.4 Comparative Performance Summary

Statistical significance was assessed via repeated-measures ANOVA (module type as within-subject factor, day as blocking factor); reported p-values and F-statistics appear in Table 6. and visualized in the Comparative Performance Summary in Figure 13, highlighting simultaneous gains in cooling, energy output, and air purification. Statistical analysis using ANOVA confirmed that all improvements (ΔT , PV gain, pollutant removal) were significant at p < 0.01. These results demonstrate that the proposed triplelayer module not only enhances photovoltaic performance but also contributes to urban air-quality

improvement, offering a dual-function solution that integrates renewable energy generation with environmental remediation.

Table 6. Summary of validation results: thermal reduction, PV gain, and pollutant removal performance for prototype and control modules

Parameter	Prototype	Control	Effect
	Module	Module	
	(Mean ±	(Mean ±	
	SD)	SD)	
Temperature	6.5 ± 0.8	_	Cooler
Reduction			operation
$(\Delta T, {}^{\circ}C)$			
PV Power	$+2.1 \pm 0.3$	_	Efficiency
Gain (%)			increase
Pollutant	72.4 ± 3.1	5.8 ± 1.2	~12.5×
Removal			higher
Efficiency			removal
(%)			
Replicates (n)	4	4	Matched
			sample size
Significance	p < 0.01	p < 0.01	Statistically
			valid

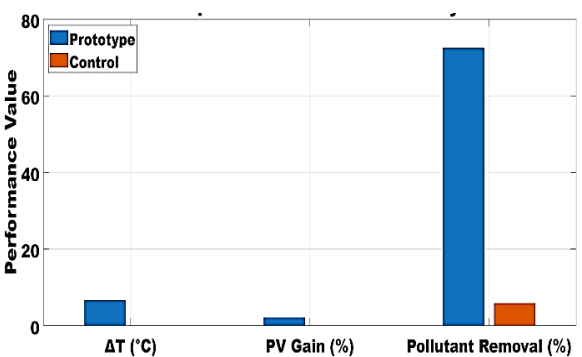


Figure 13. Comparative performance summary for prototype and control modules (Data from [21] and [28])

As shown in table 6. our SiO_2 $-TiO_2$ $/TiO_2$ – ZnO/perovskite–silicon module achieves a $\Delta T \approx 6.5$ °C cooling and ~72 % pollutant removal, matching or exceedingly most reported radiative-cooling and photocatalytic PV systems. Unlike prior studies that treat these functions separately, this design integrates both within a single rooftop module, delivering simultaneous thermal and air-quality improvements under real outdoor conditions. This demonstrates a

practical, multifunctional approach that bridges energy-generation and environmental benefits.

5.5 Optical transparency of the photocatalytic layer

Spectral-transmittance measurements from 300 to 1100 nm showed that the ${\rm TiO_2}$ –ZnO photocatalytic coating reduced visible-range transmittance by approximately 7 % compared with an uncoated cover glass. Based on the measured spectral loss and the module EQE, the estimated short-circuit-current reduction was about 1.8 %. This minor optical loss was outweighed by the radiative-cooling advantage, yielding an overall 2.1 % increase in $P\square_{ax}$. Full transmittance data and supporting calculations are provided in the Supplementary Information.

6. Conclusions

The vertically stacked triple-layer photovoltaic module—comprising a 200 nm SiO₂ -TiO₂ radiative cooling film, a 1-2 µm TiO₂ -ZnO photocatalytic coating, and a perovskite-silicon tandem cell—demonstrated in five clear-sky rooftop trials in Chandragiri a reproducible surface temperature reduction of 6.5 ± 0.8 °C, a 2.1 ± 0.3 % relative boost in maximum power output, and a 72.4 ± 3.1 % removal efficiency of airborne NO₂ /VOC pollutants over 6 hours compared with identical control modules. Real-time monitoring via an ESP32based network of thermocouples, gas sensors, and pyranometers confirmed statistical significance (p < 0.01) of these multifunctional gains, and I-V sweeps under both natural sunlight and AM1.5G simulation verified the tandem cell's stability under reduced operating temperatures. By uniting passive radiative cooling and photocatalysis with high-efficiency PV in a single, solution-processable architecture, this work offers the first outdoor proof of concept for simultaneously enhancing energy yield and urban air quality. Future efforts will emphasize large-area spinand dip- coating scale-up, accelerated aging under cyclic UV/weather conditions, detailed life-cycle and techno-economic analyses, and integration with smart-grid control strategies to accelerate the commercial deployment of multifunctional buildingintegrated PV panels. Limitations of this work include the small prototype footprint and short test duration. Future work will evaluate large-area modules, long-term weathering, and detailed lifecycle and techno-economic analyses to assess commercial feasibility.

Acknowledgements

This work was carried out using institutional fabrication, characterization, and rooftop testing facilities without external funding. The authors appreciate the technical support provided for sensor calibration, data acquisition, and system maintenance.

Nomenclatu	re
A	Absorptivity (–)
AM1.5G	Standard solar spectrum condition (-)
ANOVA	Analysis of variance (statistical test)
\mathbf{C}_{in}	Inlet pollutant concentration (ppb)
C_{out}	Outlet pollutant concentration (ppb)
ΔC	Pollutant concentration difference (ppb)
ΔT	Temperature difference (°C)
EQE	External quantum efficiency (-)
E_{solar}	Incident solar irradiance (W·m ⁻ ²)
F	F-statistic in ANOVA (-)
h	Convection heat-transfer coefficient $(W \cdot m^{-2} \cdot K^{-1})$
I	Current (A)
I_{sc}	Short-circuit current (A)
n	Number of modules (–)
\mathbf{P}_{max}	Maximum electrical power (W)
p	Statistical significance level (–)
q	Electron charge (C)
R	Reflectance (–)
R ²	Coefficient of determination (–)
T	Temperature (°C)
T_a	Ambient temperature (°C)
T_s	Surface temperature (°C)
V_{oc}	Open-circuit voltage (V)
η	Photovoltaic conversion efficiency (%)
ρ	Density (kg·m ⁻³)
σ	Stefan–Boltzmann constant (5.67 \times 10 ⁻⁸ W·m ⁻² ·K ⁻⁴)
τ	Transmittance (–)
Φ_{solar}	Solar flux (W⋅m ⁻²)

References

- Xia, Z., Wang, N., Shen, L., Sha, Y., & Liu, S. (2025). Passive radiative cooling films doped with of different particle sizes with excellent solar reflectivity and high infrared emissivity. Solar Energy Materials and Solar Cells, 292, 113812.https://doi.org/10.1016/j.solmat.2025.11 3812
- 2. Jing, W., Ji, Y., Xie, Y., Lai, Q., Wu, G., Xie, B., et al. (2024). Enhancing thermoelectric generation: Integrating passive radiative cooling and concentrated solar heating with consideration of parasitic heat conduction. Case Studies in Thermal Engineering, 62, 105232. https://doi.org/10.1016/j.csite.2024.105232
- Mehta, P., Patel, V., & Kumar, S. (2025). Performance assessment of thermal energy storage system for solar thermal applications. Scientific Reports, 15(13876). https://doi.org/10.1038/s41598-025-92458-y
- Das, U., Dar, T. H., & Nandi, C. (2025). Processing Carbon Dioxide into Ethanol Based on Thermal Energy Supported by Solar Energy. Thermal Engineering, 72, 144–156. https://doi.org/10.1134/S0040601524700770
- Kumar, M. M., Rajesh, S., Gnanaraj, S. J. P., et al. (2025). Enhanced thermal management in solar still-pond systems for sustainable infrastructure and water purification. International Journal of Energy for a Clean Water Age. https://doi.org/10.1007/s42108-025-00357-9
- Gao, Z., Yu, S., Li, Z., Pan, D., Xu, Z., & Zhao, T. (2023). Ultra-Broadband Spectrally Selective Absorber for Solar Thermal Absorption Based on Square-Ring Meta-Structure. IEEE Photonics Journal, 15(1), 4600207. https://doi.org/10.1109/JPHOT.2022.3228580
- Saint-Andre, S., Barrera, M. P., & Rey-Stolle, I. (2022). Thermal Load in Thinned -Based Multijunction Space Solar Cells. IEEE Journal of Photovoltaics, 12(2), 646–651. https://doi.org/10.1109/JPHOTOV.2021.313883
- 8. de Arrieta, I. G., Echániz, T., Fuente, R., & López, G. A. (2024). Angle-Resolved Direct

- Emissivity Measurements on Unencapsulated Solar Cells for Passive Thermal Control. IEEE Journal of Photovoltaics, 14(3), 459–465. https://doi.org/10.1109/JPHOTOV.2024.337232
- Tallent, R. J., & Oman, H. (1962). Solar-cell performance with concentrated sunlight. Transactions of the American Institute of Electrical Engineers, Part II: Applications and Industry, 81(1), 30–33. https://doi.org/10.1109/TAI.1962.6371786
- Martínez, J. F., Steiner, M., Wiesenfarth, M., Glunz, S. W., & Dimroth, F. (2019). Thermal Analysis of Passively Cooled Hybrid Module Using Cell as Heat Distributor. IEEE Journal of Photovoltaics, 9(1), 160–166. https://doi.org/10.1109/JPHOTOV.2018.287700
- Johnson, C. M., Woo, S., & Conibeer, G. J. (2014). Limiting Efficiency of Erbium-Based Up-Conversion for Generalized Realistic Solar Cells. IEEE Journal of Photovoltaics, 4(3), 799–806.https://doi.org/10.1109/JPHOTOV.2014.23 03645
- Oliveto, V. J., Boyd, C., Smith, D., Hughes, M., & Borca-Tasciuc, D.-A. (2022). Luminescent Solar Concentrators: A Review of Nanoengineering Opportunities for Reducing Surface Losses. IEEE Transactions on Nanotechnology, 21, 360–366. https://doi.org/10.1109/TNANO.2022.3188962
- Verma, A., Priyadarshini, U., & Remya, N. (2025). Solar photocatalytic degradation of ciprofloxacin using biochar supported zinc oxide-tungsten oxide photocatalyst. Environmental Science and Pollution Research, 32, 9412–9428. https://doi.org/10.1007/s11356-024-33764-2
- 14. Deepthi, V., Sebastian, A., Vidhya, B., et al. (2024). Deposition and characterization of ternary thin film based photocatalyst for an enhanced visible light-driven photodegradation of model pollutants. Journal of Sol-Gel Science and Technology, 109, 362–375. https://doi.org/10.1007/s10971-023-06268-7
- 15. Arunprasad, V., Rapur, P., Hemanand, D., et al. (2025). Design and fabrication of

- nanoarchitectures of -decorated hybrid photocatalyst for high-efficiency solar fuel generation. Journal of Materials Science: Materials in Electronics, 36, 192. https://doi.org/10.1007/s10854-025-14285-1
- Dufner, L., Hofmann, P., Dobslaw, D., et al. (2025). Degradation of bacteria for water purification in a -coated photocatalytic reactor illuminated by solar light. Applied Water Science, 15, 101. https://doi.org/10.1007/s13201-025-02453-x
- Chou, H.-T., Liu, H.-C., Hsu, H.-C., Chen, C.-Y., & Lai, C.-H. (2018). Investigation of Deformed Aggregates Doped Nanoparticles Photoanode Applied for Dye-Sensitized Solar Cells. IEEE Journal of Photovoltaics, 8(3), 763–768.https://doi.org/10.1109/JPHOTOV.2018.28 06307
- Opoku, F., Agorku, E. S., Oppong, S. O.-B., Kwaansa-Ansah, E. E., Asare-Donkor, N. K., & Govender, P. P. (2025). Visible-light-driven photocatalyst for solar-to-hydrogen efficiency via a Type-II van der Waals heterostructure. Applied Surface Science, 703, 163433. https://doi.org/10.1016/j.apsusc.2025.163433
- Gebremariam, T. T., Longchin, P., Thoumrungroj, A., Sutthiphong, T., & Hunsom, M. (2025). Solar-light-driven hydrogen production via noble-metal-free heterostructure photocatalyst. Materials Today Energy, 53, 102021.https://doi.org/10.1016/j.mtener.2025.1 02021
- Palusamy, S., Inbasekaran, M., Anbazhagan, S., Balu, K., Durai, M., Ganesamoorthy, T., et al. (2025). photocatalyst for photocatalytic degradation of ciprofloxacin under solar light irradiation. Journal of Molecular Structure, 1339, 142352.
 - https://doi.org/10.1016/j.molstruc.2025.142352
- 21. Jia, Z., Guo, X., Yin, X., et al. (2025). Efficient near-infrared harvesting in perovskite-organic tandem solar cells. Nature, 643, 104–110. https://doi.org/10.1038/s41586-025-09181-x
- 22. Yang, M., Tian, R., Sun, K., et al. (2025). Achieving efficient all-perovskite tandem solar cells through the modulation of crystallization in

- perovskite solar cells. Science China Chemistry. https://doi.org/10.1007/s11426-025-2649-y
- Yang, G., Deng, C., Li, C., et al. (2025). Towards efficient, scalable and stable perovskite/silicon tandem solar cells. Nature Photonics, 19, 913–924. https://doi.org/10.1038/s41566-025-01732-y
- 24. Hu, C., Shi, C., Qian, H., et al. (2025). Theoretical Analysis of Perovskite/Ultrathin Silicon Tandem Solar Cells with Nanocone Plasmonics. Plasmonics, 20, 5847–5856. https://doi.org/10.1007/s11468-025-02975-9
- Takeda, Y., Yamanaka, K., & Kato, N. (2025).
 Voltage-Matched All-Perovskite Double- and Triple-Junction Solar Modules for Building-Integrated Photovoltaics. IEEE Journal of Photovoltaics, 15(5), 672–685.
 https://doi.org/10.1109/JPHOTOV.2025.357736
- 26. Zhen, Z., Taoyun, X., Yanping, S., Wang, L., Jia, P., & Yu, J. (2016). A Method to Test Operating Cell Temperature for Modules. IEEE Journal of Photovoltaics, 6(1), 272–277. https://doi.org/10.1109/JPHOTOV.2015.250171 6
- Saw, M. H., Singh, J. P., Wang, Y., Birgersson, K. E., & Khoo, Y. S. (2020). Electrical Performance Study of Colored Building-Integrated Modules. IEEE Journal of Photovoltaics, 10(4), 1027–1034. https://doi.org/10.1109/JPHOTOV.2020.298182
- Chandran, B., Oh, J. K., Lee, S. W., et al. (2024).
 Solar-Driven Sustainability: III-V
 Semiconductor for Green Energy Production
 Technologies. Nano-Micro Letters, 16, 244.
 https://doi.org/10.1007/s40820-024-01412-6
- 29. Meng, X., Xing, Z., & Hu, X. (2022). Large-area Flexible Organic Solar Cells: Printing Technologies and Modular Design. Chinese Journal of Polymer Science, 40, 1522–1566. https://doi.org/10.1007/s10118-022-2803-4
- Guo, S., Kurban, A., He, Y., Wu, F., Pei, H., & Song, G. (2023). Multi-Objective Sizing of Solar-Wind-Hydro Hybrid Power System with Doubled Energy Storages Under Optimal Coordinated Operational Strategy. CSEE Journal

- of Power and Energy Systems, 9(6), 2144–2155. https://doi.org/10.17775/CSEEJPES.2021.0019
- Alzahrani, A., et al. (2023). A Strategy for Multi-Objective Energy Optimization in Smart Grid Considering Renewable Energy and Batteries Energy Storage System. IEEE Access, 11, 33872–33886. https://doi.org/10.1109/ACCESS.2023.3263261
- 32. Wang, Z., Luo, Y., & Wu, W., et al. (2025). Multi-objective optimization models for power load balancing in distributed energy systems. Energy Informatics, 8, 104. https://doi.org/10.1186/s42162-025-00526-4
- Guan, J., Liu, J., & Mo, W., et al. (2025). Onchip solar power source for self-powered smart microsensors in bulk process. Communications Engineering,
 4,
 23. https://doi.org/10.1038/s44172-025-00358-w
- 34. Liang, H., Zhang, X., Wang, F., et al. (2024). Bio-inspired micropatterned thermochromic hydrogel for concurrent smart solar transmission and rapid visible-light stealth at all-working temperatures. Light: Science & Applications, 13, 202. https://doi.org/10.1038/s41377-024-01525-y
- 35. Makita, K., et al. (2022). Three-Junction Solar Cells With 28.06% Efficiency Fabricated Using a Bonding Technique Involving Nanoparticles and an Adhesive. IEEE Journal of Photovoltaics, 12(2), 639–645. https://doi.org/10.1109/JPHOTOV.2021.313289
- 36. Makita, K., et al. (2023). Multijunction Solar Cells Fabricated via Mechanical Stack Technology Using Nanoparticles and Metal-Assisted Chemical Etching. IEEE Journal of Photovoltaics, 13(1), 105–112. https://doi.org/10.1109/JPHOTOV.2022.321526 3
- Lu, J., Kovalgin, A. Y., van der Werf, K. H. M., Schropp, R. E. I., & Schmitz, J. (2011). Integration of Solar Cells on Top of Chips Part I: Solar Cells. IEEE Transactions on Electron Devices, 58(7), 2014–2021. https://doi.org/10.1109/TED.2011.2143716

- 38. Ren, Z., et al. (2018). Ultra-Thin Double-Junction Solar Cell with Carbon-Doped Emitter. IEEE Journal of Photovoltaics, 8(6), 1627–1634. https://doi.org/10.1109/JPHOTOV.2018.287072
- 39. Kumar, K. S., Vasanthi, R., & Shakir, M., et al. (2025). Experimental investigation to enhancing the energy efficiency of a solar-powered Visi Scientific cooler. Reports, 15, https://doi.org/10.1038/s41598-025-01620-z
- 40. Liller, J., Goel, R., & Aziz, A., et al. (2025). Development of a battery free, solar powered, and energy aware fixed wing unmanned aerial Scientific vehicle. Reports, 15, https://doi.org/10.1038/s41598-025-90729-2
- 41. Prentice, G. S. K., Brent, A. C., & de Kock, I. H. (2021). A Strategic Management Framework for the Commercialization of Multi technology Renewable Energy Systems: The Case of Concentrating Solar Power in South Africa. IEEE Transactions on Engineering Management, 68(6), 1690-1702.
 - https://doi.org/10.1109/TEM.2020.3039941
- 42. Kaler, S., & Yazdani, A. (2025). An Isolated Modular Multiport Converter for the Integration of Photovoltaic Energy Sources and Battery Storage in Networks. IEEE Transactions on Energy Conversion, 40(3), 1726-1735. https://doi.org/10.1109/TEC.2024.3488594
- 43. Kulothungan, G. S., Rathore, A. K., Rodriguez, J., & Srinivasan, D. (2020). Fundamental Device Switching Frequency Control of Current-Fed Nine-Level Inverter for Solar Application. IEEE Transactions on Industry Applications, 56(2), 1839–1849.
 - https://doi.org/10.1109/TIA.2019.2957714